The formation of hybrid carbon nanomaterial by chemical vapor deposition: an efficient adsorbent for enhanced removal of methylene blue from aqueous solution

Haiyam Mohammed Alayan, Mohammed Abdulhakim Alsaadi, Rasel Das, Ali Abo-Hamad, Rusul Khaleel Ibrahim, Mohammed Khaled AlOmar and Mohd Ali Hashim

ABSTRACT

In this study, carbon species were grown on the surface of Ni-impregnated powder activated carbon to form a novel hybrid carbon nanomaterial by chemical vapor deposition. The carbon nanomaterial was obtained by the precipitation of the methane elemental carbon atoms on the surface of the Ni catalyst. The physiochemical properties of the hybrid material were characterized to illustrate the successful growth of carbon species on the carbon substrate. The response surface methodology was used for the evaluation of adsorption parameters effect such as pH, adsorbent dose and contact time on the percentage removal of MB dye from aqueous solution. The optimum conditions were found to be pH = 11, adsorbent dose = 15 mg and contact time of 120 min. The material we prepared showed excellent removal efficiency of 96% for initial MB concentration of 50 mg/L. The adsorption of MB was described accurately by the pseudo-second-order model with R^2 of 0.998 and q_e of 163.93 (mg/g). The adsorption system showed the best agreement with Langmuir model with R^2 of 0.989 and maximum adsorption capacity (Q_m) of 250 mg/g.

Key words | adsorption, carbon hybrids, chemical vapor deposition, methylene blue, powder activated carbon, response surface methodology

Haiyam Mohammed Alayan
Mohammed Abdulhakim Alsaadi (corresponding author)
Ali Abo-Hamad
Rusul Khaleel Ibrahim
Mohammed Khaled AlOmar
Mohd Ali Hashim
University of Malaya Centre for Ionic Liquids,
University of Malaya,
Kuala Lumpur 50603, Malaysia
E-mail: *mdsd68j@gmail.com*

Haiyam Mohammed Alayan
Ali Abo-Hamad
Mohd Ali Hashim
Department of Chemical Engineering,
University of Malaya,
Kuala Lumpur 50603, Malaysia

Mohammed Abdulhakim Alsaadi
Rasel Das
Nanotechnology and Catalysis Research Centre (NANOCAT),
University of Malaya,
Kuala Lumpur 50603, Malaysia

Rusul Khaleel Ibrahim
Mohammed Khaled AlOmar
Department of Civil Engineering,
University of Malaya,
Kuala Lumpur 50603, Malaysia

INTRODUCTION

Many industrial wastewater effluents, specifically those from the textile industry, account for the high concentration of methylene blue in the environment. MB has a non-biodegradable aromatic structure and it is difficult to remove from discharged effluents. This contributes to high chemical oxidation demand and poses a serious risk to human health and the aquatic system (Das *et al.* 2016).

Various techniques have been implemented to treat the dye containing wastewater, including coagulation, ion-exchange, precipitation, membrane separation, photo degradation, biological treatment and advanced oxidation processes in conjunction with biological treatments. Among these methods, the adsorption technique is regarded as a competitive and economical process due to its simplicity, ease of operation and high efficiency without producing any harmful byproducts (Peng *et al.* 2015).

Various adsorbents have been studied to determine their efficiencies for the removal of MB from aqueous streams, e.g. rice husk, montmorillonite, activated carbon, carbon nanotubes (CNTs) and graphene (Altenor *et al.* 2009; Madrakian *et al.* 2011; Liu *et al.* 2012). Carbon nanomaterials (CNMs) have been introduced as remarkable adsorbents due to their unique features, i.e. large surface area, high reactivity and rapid adsorption capability. Despite all these extraordinary properties of CNMs, the recovery of nano-structures with minimum separation steps and minimum loss of material is a serious drawback (AlSaadi *et al.* 2011).

doi: 10.2166/wst.2018.057

Generally, several schemes have been used to produce CNMs, e.g. arc discharge, laser ablation and chemical vapor deposition (CVD). However, CVD is the most promising and scalable approach. It is a versatile, cost-effective technique and produces high quantities of CNMs at low temperatures (Yamamoto *et al.* 2017). Typically, nanometer-size metal particles such as Fe, Co, and Ni are required to enable the decomposition of hydrocarbons. The CNTs produced from methane decomposition over Ni catalyst exhibited higher thermal stability than those formed using Fe catalyst (Shah & Tali 2016). Lee *et al.* reported that the maximum growth rate of CNTs was achieved when the Ni catalyst was used. They found that the diffusion rates of carbon were in the order of Ni > Fe > Co (Lee *et al.* 2002).

Hybridizing different carbon nanostructures on the surface of activated carbon (PAC) to produce material with new features appears to be a promising candidate for the removal of dyes from aqueous effluents. Unlike metallic supports, these materials retain their attachment with the substrate which eliminates the need for an additional recovery step. Moreover, the resulting hierarchical carbon combined the unique properties of CNMs with those of PAC, while maintaining chemical compatibility between these two phases. The hybridized materials have been receiving increased attention due to their unique properties; however, their application for water treatment remains to be proven (Shoukat *et al.* 2017).

Based on the preceding points, we used CVD method to prepare a hybrid carbon nanomaterial (HCNM) on PAC impregnated with Ni catalyst. The hybrid material was characterized using field emission scanning electron microscope (FESEM), transmission electron microscope (TEM), Raman spectroscopy, thermo-gravimetric analysis (TGA), Fourier transform infrared (FTIR), energy-dispersive X-ray spectroscopy (EDX), Brunauer–Emmett–Teller (BET), and zeta potential. We chose MB as a model dye to evaluate the adsorption performance of the HCNM. The response surface methodology (RSM) with central composite design (CCD) were used to optimize the effect of adsorption parameters including pH, HCNM dose, and contact time on the removal of MB. Moreover, kinetic and isotherm studies were investigated at the optimal removal conditions.

EXPERIMENTS AND METHODOLOGY

Materials and reagents

Nickel (II) nitrate hexahydrate (Ni $(NO_3)_2{\cdot}6H_2O$), PAC, MB, sodium hydroxide (NaOH), and hydrochloric acid (HCl) were purchased from Sigma Aldrich, Malaysia. All chemicals were of analytical grades.

Preparation of HCNM

Catalyst impregnation

The PAC was dried overnight at 120 °C before being impregnated with nickel (II) nitrate. The catalyst precursor was mixed with 2.0 g of PAC with a solution of 1% w/v nickel (II). The mixture was sonicated for 1 h at 60 °C and then heated in an oven at 120 °C overnight to dry out. Using the CVD tubular furnace, a two-stage thermal treatment was performed; a calcination process at 350 °C for 2 h in an N_2 atmosphere followed by reduction using H_2 gas at 550 °C for 1 h. Then the impregnated substrate (Ni-PAC) was utilized for HCNM growth (Onundi *et al.* 2011).

Synthesis of HCNM using CVD process

The HCNM was obtained on Ni-PAC via the decomposition of methane (CH_4) in a reductive atmosphere of the tubular CVD furnace. Using a temperature increase rate of 10 °C/min, the furnace was heated to 950 °C. The flow rates of H_2 and CH_4 were adjusted at 40 mL/min to provide hydrogen to methane flow ratio of 1.0. Then, the mixture of gases was passed through the reaction tube for 20 min to initiate the growth reaction.

Characterizations

The chemical composition of HCNM was analyzed using EDX. The BET surface area was determined using surface area analyzer. The morphology of HCNM was investigated using FESEM and TEM. The HCNM was characterized using Raman spectroscopy (Renishaw 2000-Spectrometer). TGA was conducted in oxygen with a heating rate of 10 °C min^{-1}. FTIR spectra were recorded by IR-21 FTIR. Ultraviolet-visible (UV-vis) measurements were conducted using UV-2300 spectrophotometer. The surface charge of HCNM suspension was conducted using a Zetasizer (Malvern).

Adsorption experiments

Experimental design and statistical analysis

The RSM/CCD method using Design Expert V7.0 software was selected to optimize the effects of the

adsorption parameters; solution pH (x_1: 3–11), HCNM dose (x_2: 5–20 mg), and contact time (x_3: 20–120 min) on the process responses; removal percentage (RV %) and HCNM adsorption capacity (Q, $mg{\cdot}g^{-1}$). The F-value and *P*-value of analysis of variance (ANOVA) were used to determine the significance of the proposed model (Dutta *et al.* 2011). A two-factor level CCD with 15 experimental runs was conducted. To achieve the highest performance, the desired responses were defined as 'maximize'. The actual parameters used in the design, the RV % and Q are listed in Tables S1 and S2 (Supporting Information, available with the online version of this paper).

Batch adsorption experiments

A convenient expression of the adsorption rate is provided by kinetic models. In the kinetic study, the optimum removal conditions suggested by the optimization study were employed in the following models: pseudo-first-order, pseudo-second-order and intraparticle diffusion. The optimum dose of HCNM was shaken at room temperature into 50 mL of a MB solution of $50\ mg{\cdot}L^{-1}$ at constant agitation speed of 180 rpm. The applied contact times were (5, 10, 15, 20, 25, 30, 40, 50, 60, 90, 120, 150, 180, and 1,440 min (24 h)). A known volume of the solution was centrifuged at 4,000 rpm for 10 min. The MB concentration in the supernatant was measured by UV-vis at absorbance wavelength of 665 nm.

The Langmuir, Freundlich, and Temkin isotherms were investigated over 10 initial concentrations of MB at the optimal removal conditions: (5, 10, 15, 20, 25, 30, 50, 60, 80, and 100 $mg\ L^{-1}$). The amount of MB uptake by HCNM, and the MB removal efficiency (%) were defined by Equations (1) and (2), respectively (Banerjee *et al.* 2014):

$$q_t = (c_o - c_t) \times \frac{V}{W} \quad (1)$$

$$\text{Removal } (\%) = \frac{C_o - C_t}{C_o} \times 100 \quad (2)$$

where q_t is the amount of MB adsorbed by HCNM ($mg{\cdot}g^{-1}$), C_o and C_t are the starting concentration of MB and the concentration after a period ($mg{\cdot}L^{-1}$), respectively, V is the initial volume of the solution (L), and W is the adsorbent weight (g).

RESULTS AND DISCUSSION

Structural characterization of HCNM

The surface morphology of the HCNM were characterized using BET, FESEM, TEM and EDX. Table 1 summarizes the BET surface area of PAC, Ni-PAC and HCNM. The PAC catalyzed the production of HCNM and enhanced the surface area from about 100 to about $165\ m^2{\cdot}g^{-1}$. The surface area of Ni-PAC was reduced due to the blockage of the PAC pores by the impregnated catalyst. Song *et al.* results show that activated carbon possesses good activity to catalyze the formation of CNTs which likely is associated with its porous structures (Song *et al.* 2010). The total pore volume of HCNM is $0.29\ cm^3{\cdot}g^{-1}$, where it was only 0.09 $cm^3{\cdot}g^{-1}$ for PAC. Given this difference, improvement of HCNM sorption capacity is expected. Allaedini *et al.*, reported that the enhancement in the adsorbent surface area was attributed to the small particle size of the impregnated catalyst (Allaedini *et al.* 2015).

FESEM and TEM images were taken for the Ni-PAC (Figure 1(a) and 1(b)). The carbon support has irregular and rough pores with well dispersed Ni particles. The TEM image of Figure 1(b) shows that catalyst was trapped successfully into PAC. The large surface area and high porosity of PAC prevent the agglomeration of the catalyst particles and provide a good catalyst distribution. The images of HCNM in Figure 1(c) and 1(d) show short CNTs embedded in the abundant porous structure of PAC. The HCNM has microstructures with groove-like features, and very similar to the surface conditions of the PAC support.

The EDX result in Figure S1 (Supporting Information, available with the online version of this paper) for HCNM confirms the successful growth of the HCNM. Most of the surface (98.6%) was carbon, but other impurities were also present, including Si and Fe (<2.0%). The Ni content had decreased from 2.0% to 0.9% after the growth.

Figure 2 shows the Raman spectra, TGA and FTIR curves. The Raman spectra for PAC, Ni-PAC and HCNM in Figure 2(a) show the D and G peaks with high intensity near 1,360 cm^{-1} and 1,590 cm^{-1}, respectively. The peak

Table 1 | Summery of BET results for PAC, Ni-PAC, and HCNM

Property	PAC	Ni-PAC	HCNM
BET surface area ($m^2{\cdot}g^{-1}$)	101.1	97.2	164.6
Total pore volume ($cm^3{\cdot}g^{-1}$)	0.09	0.07	0.29
Average pore diameter (°A)	34.89	21.29	96.19

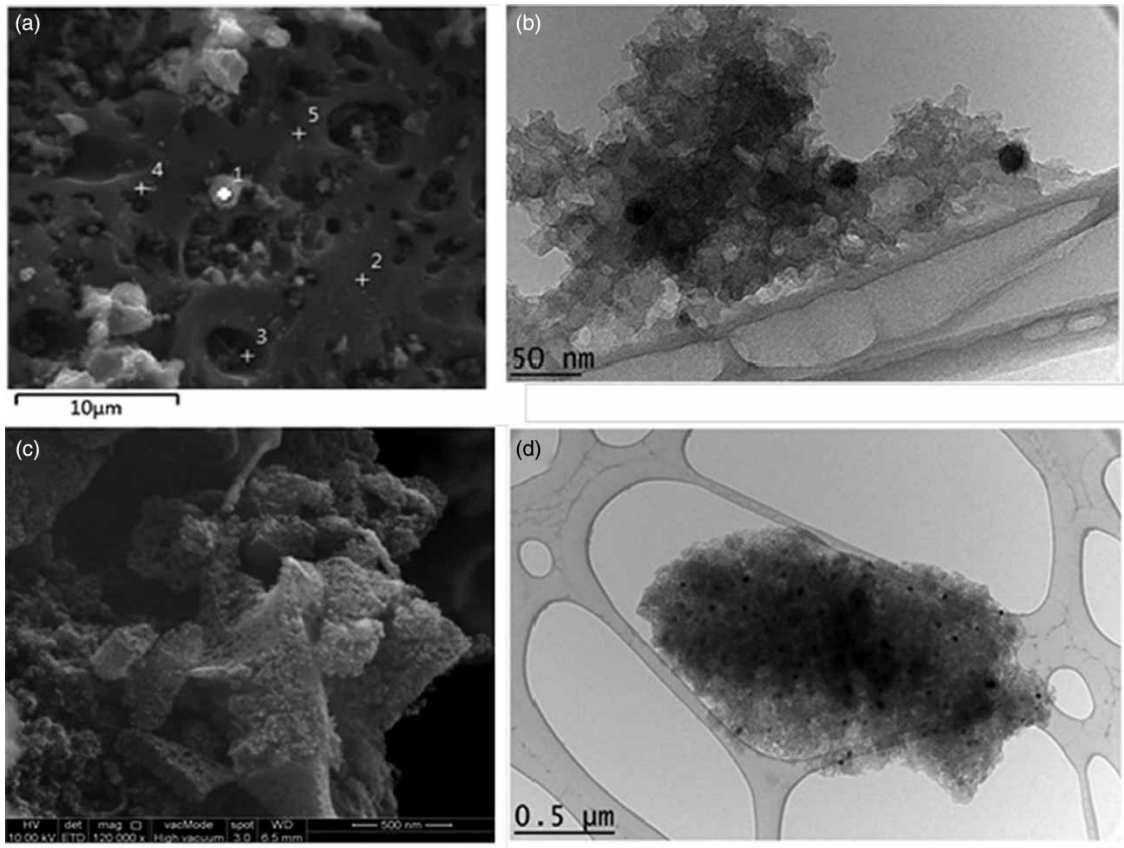

Figure 1 | FESEM and TEM images for (a) and (b) Ni-PAC before growth and (c) and (d) HCNM after growth.

near 1,360 cm^{-1} is the D band which is a defect-induced mode originated from the distorted hexagonal sp^3 carbon network (Lee *et al.* 2013). The peak near 1,590 cm^{-1} is the G band, which is reflected a typical graphite mode of C = C bonds. The extent of the carbon-containing defects of the HCNM can be evaluated by intensity of the D band to that of G band (I_D/I_G). The I_D/I_G ratio for HCNM was of 0.93, which was similar to a previously reported value (Izadi *et al.* 2011). The appearance of unusually shaped 2D peaks at 2,500 – 3,200 cm^{-1} could have been due to effects of strain on the structure (Hernandez *et al.* 2013).

The oxidation behaviour of the adsorbent was investigated using TGA. Figure 2(b) shows that PAC, Ni-PAC and HCNM exhibited single step degradation. The oxidation onset points of PAC, Ni-PAC and HCNM occurred at about 430, 490 and 510 °C, respectively. High thermal stability of HCNM at temperatures higher than 800 °C is observed through its high oxidation onset point. The weight residue for PAC sample at the end of the test was about 7 wt%, which contributed to the impurities in the substrate. This percentage increased to 21 wt% for the Ni-PAC sample after catalyst impregnation. However, the remaining weight in the HCNM sample above 650 °C was about 14 wt%. This reduction in the residual percentage was attributed to the growth of the new nanostructures on the catalyst surface, which led to a variation in the overall composition (Deshmukh *et al.* 2010).

FTIR analysis of the HCNM was used to identify the groups responsible for the adsorption of MB. Figure 2(c) shows FTIR spectra of the HCNM-MB sample. The bands at 1,400 to 1,735 cm^{-1} were assigned to the C = O stretch mode of carboxylic acid and carbonyl moieties. The bands for HCNM and HCNM-MB at 3,500 to 3,700 cm^{-1} were due to hydroxyl groups. Before the adsorption of MB, the HCNM presented the symmetric stretching vibration bands of C = O groups at 1,420 cm^{-1}, and the band at 1,580 cm^{-1} was assigned to C = C skeletal stretching. The band at about 1,110 cm^{-1} represented the C–O vibration of various oxygen-containing groups. The peaks at 2,922 and 2,855 cm^{-1} in HCNM were related to the symmetric alkane stretching of C–H bond, which become weaker after the adsorption of MB (Wang *et al.* 2015). The FTIR

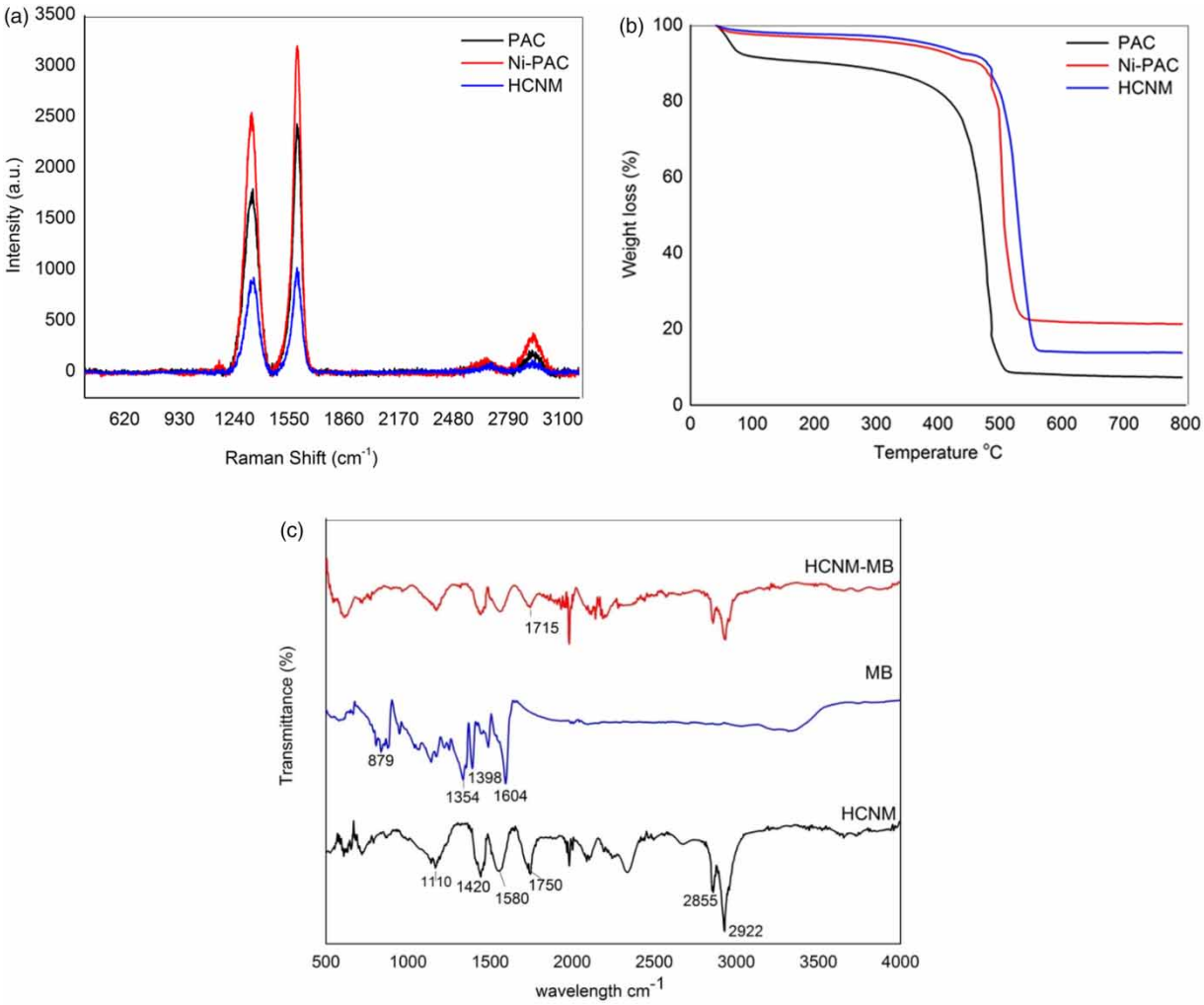

Figure 2 | (a) Raman spectra, (b) TGA curve, and (c) FTIR of HCNM before and after MB adsorption.

spectrum of free MB exhibited its ring stretch at 1,604 cm^{-1}, the symmetric stretch of C-N at 1,398 cm^{-1}, and symmetric deformation of -CH3 at 1,354 cm^{-1}. The heterocycle bending vibrations of the C–H groups of the unsaturated dimethyl-amino groups is described by the peak at 879 cm^{-1}. The peaks found in the HCNM-MB in the range of 1,200–1,500 cm^{-1} are in accordance with the peaks that originated from the spectra of MB. The ring stretching band at 1,604 cm^{-1} in the MB- free spectrum probably was shifted to 1,715 cm^{-1}, and the symmetric stretch of C–N in MB at 1,398 cm^{-1} became weaker after its adsorption onto the HCNM (Manilo *et al.* 2016).

Zeta potential is the potential difference between the stationary fluid layer attached to the adsorbent and the dispersion medium (Kyzas & Matis 2015). The HCNM exhibited a low and positive value (+9.64 mV), which suggested that the adsorbent surface had a positive charge. The pH of the zero point of charge (pH_{zpc}) for HCNM was determined by pH drift test to be 9.3. This result indicated that the adsorbent surface was positively charged at a solution pH of <9.3. Under the working conditions of pH11, the adsorbent can be considered negatively charged. This means that, in neutral to alkali media, the electrostatic interactions between the negative adsorbent and cationic MB lead to more attraction of dye molecules to the adsorbent (Fu *et al.* 2015).

Model fitting and statistical analysis

Tables S1 and S2 list the actual parameters of the experimental design runs and the responses values, (RV % and Q). The results showed that the MB removal efficiencies were between 33% and 97% and the adsorbent capacity was

between 138 and 323 mg·g^{-1}, indicating high performance of the HCNM at the studied conditions. The ANOVA for removal efficiency and adsorbent capacity are presented in Tables S3 and S4, respectively. The F-values were 20.03 and 19.36, which imply that the responses models were significant (Kumar *et al.* 2015). The *P* value was 0.0002 which also confirms that the models were highly significant. The pH and HCNM dosage were the most significant factors ($P < 0.05$). The values of the coefficients of determination (R^2) for RV % and Q were greater than 91%, which indicated a good predictability. The final proposed equations in terms of actual factors for the studied responses are as follows:

$$\text{MB removal efficiency (RV\%)} = -22.669 + 4.189\,x_1 + 11.627\,x_2 - 0.087\,x_3 - 0.223\,x_1x_2 + 0.014\,x_2x_3 - 0.346x_2^2 \quad (3)$$

$$\text{Adsorbent capacity (Q)} = 129.980 + 24.929x_1 - 2.202x_2 - 2.515\times10^{-3}x_3 - 1.357x_1x_2 - 0.046x_1x_3 + 0.039x_2x_3 \quad (4)$$

Figure S2(a) and S2(b) (available with the online version of this paper) present the theoretical and the experimental values for RV % and Q, respectively. The predicted values were quite close to the experimental values. The optimum values for MB removal using the obtained model were 11, 15 mg and 120 min for pH, adsorbent dose and reaction time, respectively. At these optimum values, a set of experiments were conducted using the procedure discussed in the experiment section. The observed removal efficiency of MB and the adsorbent capacity were about 92% and 153 mg·g^{-1}, which were close to the RSM analysis results (94% and 161 mg·g^{-1}) with a mean error <5%.

Analysis of RSM

The removal efficiency % and the adsorption capacity of HCNM over different combinations of independent variables were presented by the RSM plot as a function of two independent parameters (Figure 3). The pH and adsorbent dose were the most influential variables in MB adsorption. The removal efficiency improved as the pH was increased, reaching its maximum value at pH = 11 (Figure 3(a) and 3(b)). The pH can affect the surface charge of the adsorbent, the degree of pollutants ionization, the dissociation of functional groups on the adsorbent as well as the structure of the dye molecule. Hence, the higher removal of MB that was observed at pH11 can be explained by the deprotonation of some functional groups resulting in more negatively charged surface ($pH > pH_{pzc}$). Also, more dissociation of the MB molecules (pKa = 3.8 for MB) occurred at high pH values which enhanced the electrostatic attraction between the HCNM and the MB molecules. On the other hand, in acidic solutions, the competitive effects of excess H^+ and the electrostatic repulsion between the cationic dye would result in a decrease in the removal efficiency of the dye (Ai *et al.* 2011).

Figure 3(c) and 3(d) show that, at constant pH values, the adsorbent capacity and its removal efficiency were increased as the amount of adsorbent increased. The significant effect of the HCNM dosage on both responses was confirmed by the high F-values (98.22 and 64.63) presented in Tables S3 and S4, respectively (available with the online version of this paper). The adsorption enhancement could be due to the availability of more adsorption sites. Conversely, at low dosages, the removal percentage decreased significantly because longer time is required for the adsorption process to reach equilibrium due to the reduction of reactive sites with respect to the dye molecules (Krishni *et al.* 2014). The effect of the interaction between the pH and the adsorbent dosage (x_1 x_2) was also valuable on the adsorbent capacity since it exhibited an F-value of 19.43.

Kinetic studies

Kinetic analyses were conducted at the optimal removal conditions using pseudo-first-order and pseudo-second-order, as well as intraparticle diffusion. Table S5 (available online) summarizes the related equations and the characteristic parameters. In the linear form of the pseudo-first-order model, q_e and q_t are the amounts of the adsorbed MB at equilibrium and at time t, respectively, and K_1 is the adsorption rate constant. The pseudo-second-order rate constant of adsorption K_2 and q_e were determined from the slope and intercept of plots of t/q_t versus t (Figure 4). The removal rate is designated by the square root of time in the intraparticle diffusion (ID). The values of q_e and K_1 in Table S5 were obtained from the intercept and slope of the plot of ln (q_e-q_t) versus t (Figure S3(a)) (Figure S3 is available online). The values of the ID rate constant, K_d and the thickness of the boundary layer in terms of c values were depicted from the slope and intercept of the plot of q_t vs. $t^{0.5}$ (Figure S3 (b)). As seen from Figure S3(b) the ID plot was not linear over whole time range and did not pass through the origin. This indicates the participation of ID in the

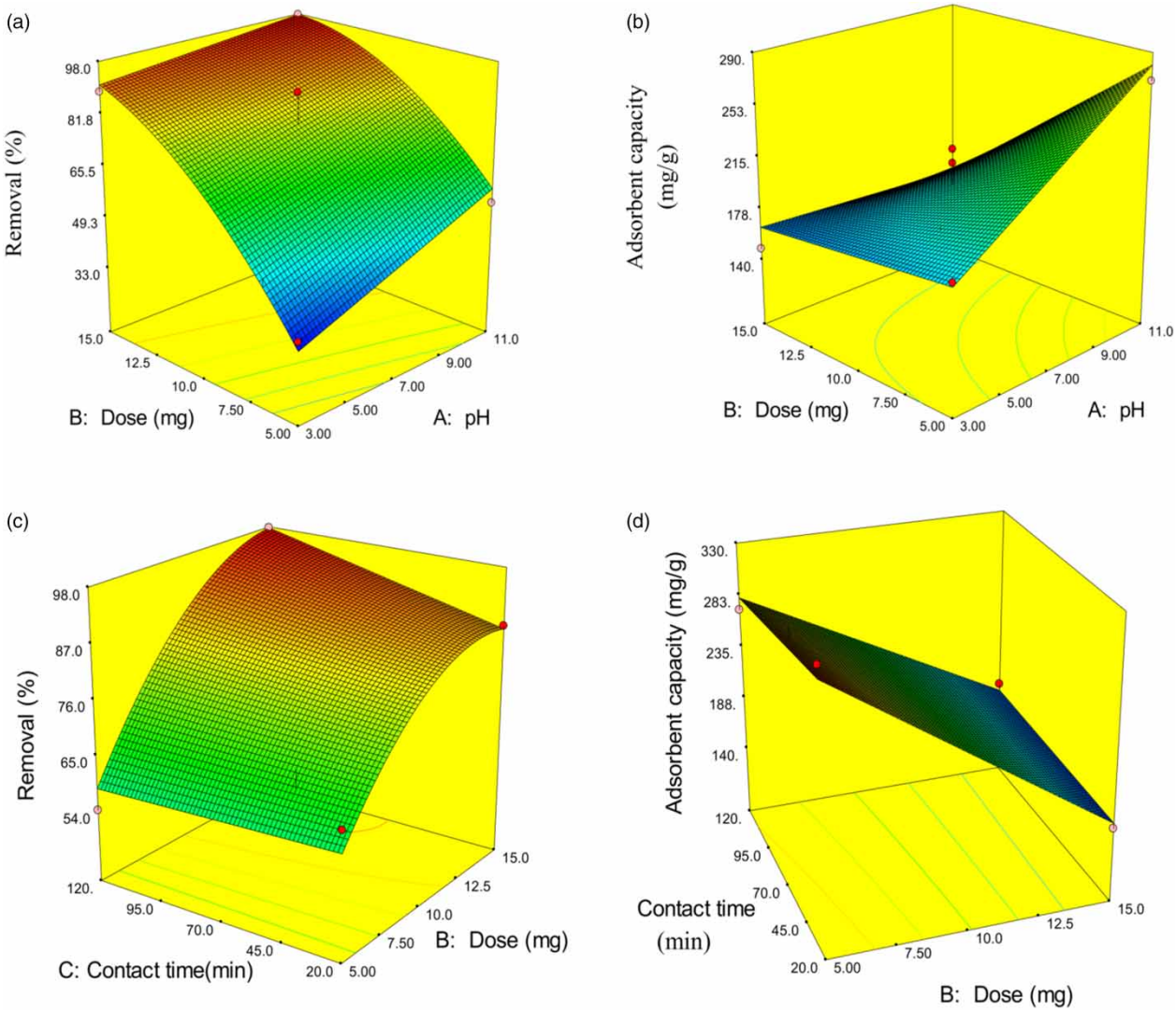

Figure 3 | RSM plots of MB removal efficiency and adsorbent capacity considering the effect of (a) and (b) pH and dose and (c) and (d) contact time and HCNM dose.

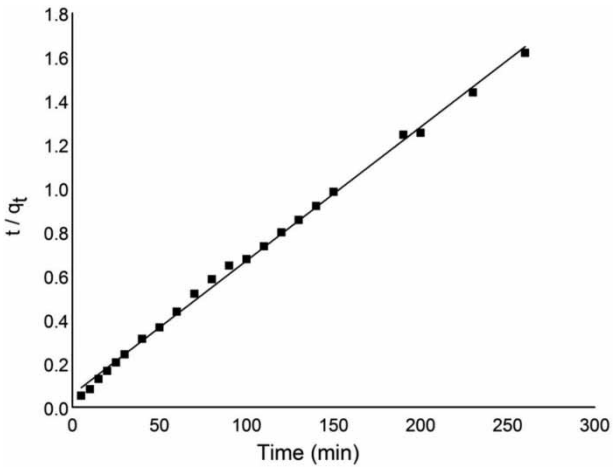

Figure 4 | Pseudo-second-order kinetic model fitting of MB adsorption on HCNM at optimum conditions.

adsorption process but it was not the only rate-controlling step (Zhang *et al.* 2015).

The chi-squared statistic (X^2) is expressed in Equation (5):

$$X^2 = \sum \frac{\left(q_{eexp-}\ q_{ecal}\right)2}{q_{ecal}} \tag{5}$$

where $q_{e,exp}$ and $q_{e,cal}$ are the experimental and calculated adsorption capacities of HCNM ($mg{\cdot}g^{-1}$), respectively. The kinetic model provides a good fit of the experimental data when the value of R^2 was high and the value of X^2 was low (Table S5) shows that the pseudo-second-order model provided a better fit of the MB removal with the highest R^2 value, and the smallest X^2 value, i.e. 0.998 and 5.75. This finding was in agreement with some other kinetic results for MB

adsorption on carbonaceous adsorbents (Li *et al.* 2013; Park *et al.* 2016). The applicability of the pseudo-second-order model suggests the possibility of adsorbate and adsorbent involvement in the adsorption mechanism and the adsorption rate was controlled by chemisorption involving valence forces through exchange or sharing electrons (Bhatti *et al.* 2017).

Isotherm studies

The equilibrium adsorption data were tested using Langmuir, Freundlich and Temkin models. Table S6 (available online) summarized the coefficients of the different isotherms. In the linearized form of Langmuir equation, C_e is the equilibrium concentration of MB, and q_e is the amount of MB adsorbed per unit mass of the adsorbent. K_L and Q_m are adsorption equilibrium constant and the maximum adsorption capacity, respectively. The value of the dimensionless constant parameter (R_L) described by Equation (6) can be used to predict the type of Langmuir isotherm: unfavourable ($R_L > 1$), linear ($R_L = 1$), favourable ($0 < R_L < 1$) or irreversible ($R_L = 0$) (Zhang *et al.* 2015).

$$R_L = \frac{1}{1 + K_L C_i} \tag{6}$$

where c_i is the highest dye concentration ($mg \cdot L^{-1}$).

Freundlich isotherm constants are presented by K_F and n and determined from the intercept and slope of the plot of ln q_e versus ln C_e (Figure S4(a), available online). The distribution coefficient, K_F, represents the amount of MB adsorbed by HCNM per a unit equilibrium concentration. The heterogeneity of the adsorbent surface and the adsorption favourability were evaluated by the magnitude of 1/n. As this value approaches zero, it indicates that the adsorbent surface is becoming more heterogeneous (Tahir *et al.* 2017). The Temkin isotherm is characterized by uniform distribution of the binding energies. In the equation, B and K_T were determined from the slope and intercept of the linearized plot of q_e vs. ln C_e (Figure S4(b)). B (dimensionless) = RT/b, where b is the Temkin constant related to the heat of adsorption ($J \cdot mol^{-1}$), R is the universal gas constant, T is the absolute temperature in Kelvin, and K_T is the Temkin equilibrium binding constant.

The results in Table S6 show the adsorption favourability of MB onto HCNM confirmed by the constants of Langmuir and Freundlich isotherms ($R_L = 0.031$ and $n = 2.9$). The respectful MB removal demonstrated by Freundlich model assumes the presence of non-equivalent binding sites in the heterogenous surface energy system. A similar result was obtained for MB removal onto low cost biowaste (Krishni *et al.* 2014). However, Langmuir isotherm provided the best fit (Figure 5) with the highest R^2 at maximum adsorption capacity of 250 $mg \cdot g^{-1}$. This suggests the occurrence of monolayer adsorption of MB at the homogeneous sites of the HCNM surface.

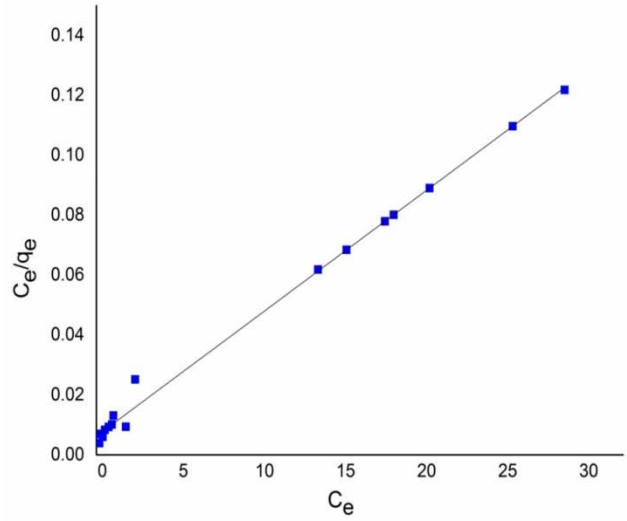

Figure 5 | Langmuir isotherm plot for MB adsorption on HCNM at optimum conditions.

The validity of the models was also determined by calculating the standard deviation (S.D. %) using Equation (7):

$$S.D.\% = \sqrt{\frac{\sum (q_{exp} - q_{cal})/q_{exp}}{n - 1}} \tag{7}$$

where the subscripts exp and cal refer to the experimental and the calculated data, respectively, and n is the number of data points. The smallest value of S.D. for Langmuir model indicated that this isotherm is the best model which can describe the adsorption of MB on HCNM adsorbent. Table S7 (available online) shows a comparison of the maximum adsorption capacity of MB on different reported adsorbents. In comparison with previous works, HCNM can be considered as a promising adsorbent for MB removal from aqueous solution.

CONCLUSION

In this study, a novel sorbent and a simple pathway was used to synthesize HCNM with multiscale structure. The as-synthesized HCNM exhibited good graphitic structure and

excellent sorption capacity. In alkaline medium, at pH of 11, excellent removal of MB was achieved. The RSM/CCD design effectively optimized the adsorption parameters such as pH, adsorbent dose and contact time. Based on the optimization studies, the adsorption of MB was highly dependent on the pH of solution, and the adsorbent surface charge. The adsorption kinetics and isotherms studies demonstrated that the adsorption process obeyed the pseudo-second-order kinetics and Langmuir isotherm model, respectively. The as-synthesized HCNM exhibited maximum adsorption capacity of 250 $mg \cdot g^{-1}$. The produced HCNM can be used directly in adsorption processes without removing the substrate from the collected product, unlike other CNMs prepared on metal substrates. The main strength of MB adsorption is the electrostatic interaction, while the π-π stacking interaction between the aromatic backbone of the dye and the graphene planes of the HCNM might also contribute to the whole interaction. The results of the present investigation indicate that HCNM is a potential adsorbent for methylene blue removal from aqueous solutions.

ACKNOWLEDGEMENTS

The authors express their thanks to the University of Malaya UMRG (RP017A-13AET) for providing a Postgraduate Research Grant (PG243-2015B) to fund this research.

REFERENCES

Ai, L., Zhang, C., Liao, F., Wang, Y., Li, M., Meng, L. & Jiang, J. 2011 Removal of methylene blue from aqueous solution with magnetite loaded multi-wall carbon nanotube: kinetic, isotherm and mechanism analysis. *Journal of Hazardous Materials* **198**, 282–290.

Allaedini, G., Tasirin, S. M. & Aminayi, P. 2015 Synthesis of Fe–Ni–Ce trimetallic catalyst nanoparticles via impregnation and co-precipitation and their application to dye degradation. *Chemical Papers* **70** (2), 231–242.

AlSaadi, M. A., Al-Mamun, A., Muyibi, S. A., Alam, M. Z., Sopyan, I., Atieh, M. A. & Ahmed, Y. M. 2011 Synthesis of various carbon nanomaterials (CNMs) on powdered activated carbon. *African Journal of Biotechnology* **10** (81), 18892–18905.

Altenor, S., Carene, B., Emmanuel, E., Lambert, J., Ehrhardt, J.-J. & Gaspard, S. 2009 Adsorption studies of methylene blue and phenol onto vetiver roots activated carbon prepared by chemical activation. *Journal of Hazardous Materials* **165** (1), 1029–1039.

Banerjee, S., Sharma, G. C., Chattopadhyaya, M. C. & Sharma, Y. C. 2014 Kinetic and equilibrium modeling for the adsorptive removal of methylene blue from aqueous solutions on of activated fly ash (AFSH). *Journal of Environmental Chemical Engineering* **2** (3), 1870–1880.

Bhatti, H. N., Jabeen, A., Iqbal, M., Noreen, S. & Naseem, Z. 2017 Adsorptive behavior of rice bran-based composites for malachite green dye: isotherm, kinetic and thermodynamic studies. *Journal of Molecular Liquids* **237** (Supplement C), 322–333.

Das, R., Hamid, S. B. A. & Annuar, M. S. M. 2016 Highly efficient and stable novel nanoBiohybrid catalyst to avert 3, 4-dihydroxybenzoic acid pollutant in water. *Scientific Reports* **6**, 33572.

Deshmukh, A. A., Mhlanga, S. D. & Coville, N. J. 2010 Carbon spheres. *Materials Science and Engineering: R: Reports* **70** (1–2), 1–28.

Dutta, S., Bhattacharyya, A., Ganguly, A., Gupta, S. & Basu, S. 2011 Application of response surface methodology for preparation of low-cost adsorbent from citrus fruit peel and for removal of Methylene Blue. *Desalination* **275** (1), 26–36.

Fu, J., Chen, Z., Wang, M., Liu, S., Zhang, J., Zhang, J., Han, R. & Xu, Q. 2015 Adsorption of methylene blue by a high-efficiency adsorbent (polydopamine microspheres): kinetics, isotherm, thermodynamics and mechanism analysis. *Chemical Engineering Journal* **259**, 53–61.

Hernandez, J. M. M., San German, C. M. R., Arceo, L. D. B., Villalobos, L. Z. & Flores, M. E. 2013 Synthesis and characterization of carbon nanospheres obtained by microwave radiation. *Carbon* **54**, 168–174.

Izadi, N., Rashidi, A. M., Horri, B. A., Mosoudi, M. R., Bozorgzadeh, H. R. & Zeraatkar, A. 2011 Growth of single-walled carbon nanotubes on a Co–Mo–MgO supported catalyst by the CVD of methane in a fixed bed reactor: model setting and parameter estimation. *Solid State Sciences* **13** (6), 1242–1250.

Krishni, R., Foo, K. & Hameed, B. 2014 Adsorption of cationic dye using a low-cost biowaste adsorbent: equilibrium, kinetic, and thermodynamic study. *Desalination and Water Treatment* **52** (31–33), 6088–6095.

Kumar, M., Tamilarasan, R., Arthanareeswaran, G. & Ismail, A. F. 2015 Optimization of methylene blue using Ca^{2+} and Zn^{2+} bio-polymer hydrogel beads: a comparative study. *Ecotoxicology and Environmental Safety* **121**, 164–173.

Kyzas, G. Z. & Matis, K. A. 2015 Nanoadsorbents for pollutants removal: a review. *Journal of Molecular Liquids* **203**, 159–168.

Lee, C. J., Park, J. & Jeong, A. Y. 2002 Catalyst effect on carbon nanotubes synthesized by thermal chemical vapor deposition. *Chemical Physics Letters* **360** (3), 250–255.

Lee, S., Hong, J., Koo, J. H., Lee, H., Lee, S., Choi, T., Jung, H., Koo, B., Park, J. & Kim, H. 2013 Synthesis of few-layered graphene nanoballs with copper cores using solid carbon source. *ACS Applied Materials & Interfaces* **5** (7), 2432–2437.

Li, Y., Du, Q., Liu, T., Peng, X., Wang, J., Sun, J., Wang, Y., Wu, S., Wang, Z., Xia, Y. & Xia, L. 2013 Comparative study of methylene blue dye adsorption onto activated carbon, graphene oxide, and carbon nanotubes. *Chemical Engineering Research and Design* **91** (2), 361–368.

Liu, T., Li, Y., Du, Q., Sun, J., Jiao, Y., Yang, G., Wang, Z., Xia, Y., Zhang, W. & Wang, K. 2012 Adsorption of methylene blue from aqueous solution by graphene. *Colloids and Surfaces B: Biointerfaces* **90**, 197–203.

Madrakian, T., Afkhami, A., Ahmadi, M. & Bagheri, H. 2011 Removal of some cationic dyes from aqueous solutions using magnetic-modified multi-walled carbon nanotubes. *Journal of Hazardous Materials* **196**, 109–114.

Manilo, M., Lebovka, N. & Barany, S. 2016 Mechanism of methylene blue adsorption on hybrid laponite-multi-walled carbon nanotube particles. *Journal of Environmental Sciences* **42**, 134–141.

Onundi, Y. B., Mamun, A., Al Khatib, M., Al Saadi, M. & Suleyman, A. 2011 Heavy metals removal from synthetic wastewater by a novel nano-size composite adsorbent. *International Journal of Environmental Science and Technology (IJEST)* **8** (4), 799–806.

Park, J.-A., Kim, J.-H., Kang, J.-K., Son, J.-W., Yi, I.-G., Kim, S.-B., Lee, S.-H., Choi, J.-W. & Lee, C.-G. 2016 Determination of optimum isotherm and kinetic models for phosphate sorption onto iron oxide nanoparticles: nonlinear regression with various error functions. *Desalination and Water Treatment* **57** (7), 3107–3118.

Peng, Q., Liu, M., Zheng, J. & Zhou, C. 2015 Adsorption of dyes in aqueous solutions by chitosan–halloysite nanotubes composite hydrogel beads. *Microporous and Mesoporous Materials* **201**, 190–201.

Shah, K. A. & Tali, B. A. 2016 Synthesis of carbon nanotubes by catalytic chemical vapour deposition: a review on carbon sources, catalysts and substrates. *Materials Science in Semiconductor Processing* **41**, 67–82.

Shoukat, S., Bhatti, H. N., Iqbal, M. & Noreen, S. 2017 Mango stone biocomposite preparation and application for crystal violet adsorption: a mechanistic study. *Microporous and Mesoporous Materials* **239** (Supplement C), 180–189.

Song, J., Feng, S., Zhao, J., Zheng, J. & Zhu, Z. 2010 Activated carbon catalyzing the formation of carbon nanotubes. *Materials Research Bulletin* **45** (9), 1234–1239.

Tahir, N., Bhatti, H. N., Iqbal, M. & Noreen, S. 2017 Biopolymers composites with peanut hull waste biomass and application for Crystal Violet adsorption. *International Journal of Biological Macromolecules* **94** (Part A), 210–220.

Wang, W., Wang, F., Kang, Y. & Wang, A. 2015 Enhanced adsorptive removal of methylene blue from aqueous solution by alkali-activated palygorskite. *Water, Air, & Soil Pollution* **226** (3), 1–13.

Yamamoto, Y., Inoue, S. & Matsumura, Y. 2017 Thermal decomposition products of various carbon sources in chemical vapor deposition synthesis of carbon nanotube. *Diamond and Related Materials* **75**, 1–5.

Zhang, Z., Wang, W. & Wang, A. 2015 Highly effective removal of methylene blue using functionalized attapulgite via hydrothermal process. *Journal of Environmental Sciences* **33**, 106–115.

First received 17 September 2017; accepted in revised form 25 January 2018. Available online 12 February 2018